ACS OMEGA

http://pubs.acs.org/journal/acsodf

Perspective

Investigating the $A_{n+1}B_nX_{3n+1}$ Homologous Series: A New Platform for Studying Magnetic Praseodymium Based Intermetallics

Trent M. Kyrk, Moises Bravo, Gregory T. McCandless, Saul H. Lapidus, and Julia Y. Chan*

Cite This: *ACS Omega* 2022, 7, 19048−19057

Read Online

ACCESS | Metrics & More | Article Recommendations | Supporting Information

ABSTRACT: The recent discovery of the $A_{n+1}B_nX_{3n+1}$ (A = lanthanide, B = transition metal, X = tetrel) homologous series provides a new platform to study the structure−property relationships of highly correlated electron systems. Several members of $Ce_{n+1}Co_nGe_{3n+1}$ (n = 1, 4, 5, 6, and ∞) show evidence of heavy electron behavior with complex magnetic interactions. While the Ce analogues have been investigated, only n = 1, 2, and ∞ of $Pr_{n+1}Co_nGe_{3n+1}$ have been synthesized, with n = 1 and 2 showing a nonsinglet magnetic ground state. The Pr analogues can provide a platform for direct comparison of highly correlated behavior. In this perspective, we discuss the impetus for synthesizing the $Pr_{n+1}Co_nGe_{3n+1}$ members and present the structural characterization of the n = 3 and n = 4 members. We lay the foundation for future investigations of the $Pr_{n+1}Co_nGe_{3n+1}$ family of compounds and highlight the importance of complementary methods to characterize new quantum materials.

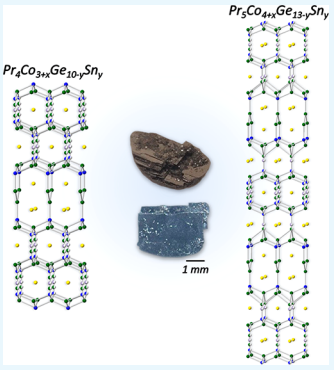

1. INTRODUCTION

The discovery of novel emergent electronic states in magnetic highly correlated quantum materials[1,2] is necessary to advance next generation technologies.[3] These states allow the stabilization of a number of quasi-particles that can be taken advantage of for new technologies or advance our understanding of important physical phenomena, such as Majorana fermions in topological insulators for quantum computing,[4,5] Weyl fermionic states in topological semimetals to study magnetotransport phenomena,[6] and other highly correlated states.[3,4,7−9] Herein, we focus on heavy fermions and their quantum critical points, around which unconventional superconductivity has been observed.[10,11] From a materials perspective, our goals are to (1) connect highly correlated physics to the structural and electronic features of a material, (2) identify and synthesize quantum materials, and (3) understand the synthesis of quantum materials. These goals aim to discover new platforms of compounds with magnetic and transport properties that can be tuned to study quantum critical points.[10] While external parameters such as temperature, pressure, and magnetic field are necessary in these investigations, additional parameters such as dimensionality and the structural environment of magnetic ions can enrich our understanding of structure−property relationships.

Occasionally, homologous series, families of related compounds with a chemical formula that changes as a function of an integer, are discovered that allow a robust method of tuning physical properties through discrete variations in chemical structure and composition. These families can be built from intergrowth structures, where each member is rationalized as an assembly of known crystal structures. In recent decades, several intermetallic homologous series have been discovered such as Ce_nMIn_{3n+2},[12,13] $Th_2(Au_xSi_{1-x})[AuAl_2]_nSi_2$,[14] $Ce(PdAl)_n$,[15] and $[LnGe_2]_n[LnLi_2Ge]_m$.[16,17] The nature of a homologous series makes them specially systematic to study complex phenomena as linked to their repeating structural motifs, thus allowing novel connections to be drawn between chemical structure and properties in ways dissimilar compounds cannot achieve. The $Ln_{2-y}Zn_4As_4{\cdot}n(LnAs)$ (Ln = La−Nd, Sm, and Gd) series built from [LnAs] and $[Zn_2As_2]$ slabs[18] is an example of band gap tuning as a function of structure. Here, there is a gradual increase in electron density at the band gap as a function of the [LaAs] slabs' thickness, directly attributed to the change in structure and composition. Ce_nMIn_{3n+2} (n = 1, 2, and ∞; M = Co, Rh, and Ir) offered new potential in studying magnetically mediated superconductivity in the $CeIn_3$ parent structure,[19] $CeMIn_5$,[20,21] and Ce_2MIn_8[22] by considering the role of the $CeIn_3$ and MIn_2 layers and transition metal substitution. To evaluate the highly correlated nature of compounds, the Sommerfeld coefficient (γ), the electronic contribution to specific heat, and a measure of heavy electron behavior can be obtained from the following equation: $C_p = \gamma T + \alpha T^3$, where T is the temperature and α is the phonon contribution to the specific heat. With application of pressure, the antiferromagnets emerge into a superconducting phase,[13] with an enhanced Sommerfeld coefficient of $\gamma \sim 400$ mJ/mol K^2 for Ce_nRhIn_{3n+2} (n = 1 and 2)

Received: April 6, 2022
Accepted: May 4, 2022
Published: June 3, 2022

and $\gamma \sim 700$ mJ/mol K^2 for Ce_nIrIn_{3n+2} (n = 1 and 2) and, most prominently, with the antiferromagnetic $CeIn_3$ (T_N = 10 K) becoming superconducting with 27.5 kbar. The properties of this family of compounds led to the linking of dimensionality, in addition to the evaluation of the significance of the Ce local cuboctahedral environment on the influence of magnetic correlation. Given a new intermetallic homologous series, we present a robust platform to demonstrate the potential for the discovery of new phenomena and the study of exotic and emergent behavior as a function of dimensionality.

2. $A_{N+1}Co_NGe_{3N+1}$

The $A_{n+1}B_nX_{3n+1}$ homologous series (A = lanthanide, B = transition metal, X = tetrel)[23] holds promise as a new platform to study highly correlated emergent phenomena. The progression of the series can be understood as systematic additions of $BaNiSn_3$/$AuCu_3$-type disordered subunits intergrown with $CeNiSi_2$-type subunits, where odd and even members crystallize in the orthorhombic *Cmcm* and *Cmmm* space groups, respectively. For each n member of the series, $n - 1$ $BaNiSn_3$/$AuCu_3$-type subunits are stacked along the b direction between $CeNiSi_2$-type subunits, where the sequential stacking of $BaNiSn_3$/$AuCu_3$ subunits separates the $CeNiSi_2$ subunits as a function of n. Therefore, the homologous series provides a systematic platform to study the effects of changing dimensionality and local environment on magnetism and electronic structure.

$Ce_{n+1}Co_nGe_{3n+1}$ compounds n = 1,[24] 4,[25,26] 5,[27] 6,[28] and ∞[29] have been reported and can be used to study the interplay of local $4f^1$ electron systems and conduction electrons. Ce^{3+} ions are odd spin systems that follow Kramer's theorem, which guarantees the formation of a doublet electronic ground state outside of an applied magnetic field due to the presence of time reversal symmetry. At sufficiently low temperatures, the doublet ground state allows for local 4*f* and conduction electron hybridization that results in the emergence of the magnetic Kondo effect, manifesting as heavy electron behavior, and eventually a valence transition from Ce^{3+} to Ce^{4+}.[30] As illustrated by the Doniach model,[31] Kondo interactions are in direct competition with Ruderman−Kittel−Kasuya−Yosida (RKKY) interactions dependent upon the strength of magnetic exchange interactions, making compounds that exhibit both heavy electron behavior and magnetic ordering exciting platforms for studying quantum critical points. All characterized members of the $Ce_{n+1}Co_nGe_{3n+1}$ family, n = 1, 4, 5, 6, and ∞, show evidence of heavy electron behavior, and the n = 4, 5, 6, and ∞ members demonstrate complex anisotropic competition between antiferromagnetic and ferromagnetic states.

The n = 1 member, $CeCo_{0.89}Ge_2$, is a Kondo compound (T_K > 200 K) with no magnetic ordering down to 1.5 K.[32−34] However, patterns have emerged in the properties of the $Ce_{n+1}Co_nGe_{3n+1}$ family for n = 4−6. The anisotropic magnetic properties of $Ce_5Co_{4+x}Ge_{13}$, $Ce_6Co_{5+x}Ge_{16}$, and $Ce_7Co_{6+x}Ge_{19}$ are similar to one another. Two of the five magnetic transitions of the n = 6 member overlap with two of the transitions in the n = 4 member, with the remaining three transitions overlapping with the transitions found in the n = 5 member, most likely due to their related local environments.[26−28] The n = ∞ member, $CeCoGe_3$, is a Kondo antiferromagnet ($T_K \sim 100$ K) with three magnetic transitions at T = 21 K, T = 12 K, and T = 8 K[35] that resemble the anisotropy of the other n members. The presence of $CeCoGe_3$ in this series is particularly exciting, as the noncentrosymmetric superconductor has recently been theoretically predicted to be topologically nontrivial.[36−38]

Topological phases containing local inversion symmetry breaking such as UTe_2[39,40] and $CeRh_2As_2$[41,42] have gathered much attention in recent years. As such, the $CeCoGe_3$ sublattice in $Ce_{n+1}Co_nGe_{3n+1}$ creates a unique opportunity to understand the structure−property relationships of local inversion symmetry breaking on the bulk properties of a material as a function of n.[43,44] With evidence of highly correlated phenomena, complex magnetism, and the potential for topological behavior, the $Ce_{n+1}Co_nGe_{3n+1}$ family of compounds are candidates to study new states of matter, such as Weyl−Kondo semimetals,[7,45] through the addition of $CeCoGe_3$ layers. The potential of the $A_{n+1}B_nX_{3n+1}$ series is not limited to the Ce analogues, as the physical properties of Pr based intermetallic compounds have garnered increasing interest over the past three decades.

3. $PR_{N+1}Co_NGe_{3N+1}$

Ce and Pr behave fundamentally differently due to their respective $4f^1$ and $4f^2$ electronic configurations. For example, CeAlGe is an incommensurate antiferromagnetic type-I Weyl semimetal,[46] whereas PrAlGe exhibits type-II Weyl semimetal behavior with an anomalous Hall conductivity of ∼680 Ω^{-1} cm^{-1} due to a ferromagnetic spin−glass-like ordering at 15 K.[47,48] Observations of Weyl fermions through angle resolved photoelectron spectroscopy measurements and the intrinsic anomalous Hall response confirmed these differences in physical properties.[49,50] Additionally, Si substitution in $PrAlGe_{1-x}Si_x$ ($0 < x < 1$) has shown tunable anomalous Hall effects, demonstrating the interplay between scattering mechanism and topological state. Magnetoresistance sensitivity was also shown to increase by as much as 100% from PrAlSi to PrAlGe.[51]

The 4*f* electronic ground states are responsible for differences in physical properties through changes in their interaction with conduction electrons. While Ce^{3+} ions follow Kramer's theorem, Pr^{3+} ions have an even number of 4*f* electrons and are classified as non-Kramer's ions. Here, the doublet ground state is no longer protected by time reversal symmetry, resulting in many Pr compounds adopting a singlet ground state and, thus, having neither heavy electron behavior nor magnetic ordering; for example, $PrCoGe_3$ is non-Kondo with no magnetic ordering.[52] However, the point group symmetry of the local environment of non-Kramer's ions affords another path to achieving a doublet or quasi-doublet ground state through crystal electric field (CEF) splitting, inspiring the study of quantum fluctuations in spin systems and exotic quadrupolar phenomena.[53] Crystal field schemes of Pr atoms in cubic environments have been the primary focus of the highly correlated behavior in Pr systems due to their predilection toward doublet ground states. The CEF stabilized non-Kramer's doublet ground state results in a two-channel Kondo effect through electric quadrupolar ordering.[54] Electric quadrupolar ordering has led to identification of new quantum critical points,[55] non-Fermi liquid behavior,[56] and unconventional superconductivity.[57] $PrInAg_2$[58,59] was the first heavy electron Pr compound discovered with the second largest Sommerfeld coefficient identified ($\gamma \sim 6.5$ J/mol K^2). Later, a large family of heavy superconducting compounds, PrM_2X_{20} (M = Ti and V with X = Al;[56] M = Ir and Rh with X = Zn;[60,61] M = Ni with X = Cd[62]), was identified where the different M and X could be varied to tune the superconducting transition temperatures, quadrupolar order, and magnetic order.

Nonetheless, compounds with lower Pr point symmetry have recently shown that heavy electron behavior of a similar

https://doi.org/10.1021/acsomega.2c02152
ACS Omega 2022, 7, 19048−19057

magnitude can be observed in quasi-doublet states. In PrSi,[63] ferromagnetic ordering is observed despite a singlet ground state, due to quasi-doublet formation via a singlet ground state to singlet first excited state transition with a difference in energy of ΔT = 9 K. Low-lying crystal field excitations with ΔT = 12 K were also used to justify the elevated Sommerfeld coefficient of $Pr_2Rh_3Ge_5$, $\gamma \sim 81$ mJ/mol K^2.[64] The singlet−singlet quasi-doublets (ΔT = 63.9 K) in PrPdAl[65] were recently found to result in a raised Sommerfeld coefficient of $\gamma \sim 940$ mJ/mol K^2. With these examples and others, such as $Pr_3Rh_4Sn_{13}$ ($\gamma \sim 761$ mJ/mol K^2)[66] and $Pr_5Ir_4Sn_{10}$ ($\gamma \sim 500$ mJ/mol K^2),[67,68] there is mounting interest in Pr based intermetallic compounds with noncubic point symmetries and highly correlated behavior that, when coupled with the modularity of a homologous series, supports investigation of the $Pr_{n+1}Co_nGe_{3n+1}$ series.

In the $Pr_{n+1}Co_nGe_{3n+1}$ series, n = 1, 2, and ∞ members have been reported. $PrCo_{1-x}Ge_2$, n = 1, has one antiferromagnetic transition at 5 K and a potential metamagnetic transition in the low-field magnetization.[69] For $Pr_3Co_{2+x}Ge_7$,[70] n = 2, magnetic susceptibility data at 0.1 T shows two antiferromagnetic transitions at 5.3 and 9.3 K and three metamagnetic transitions below an applied field of 3 T. These transitions seem to be suppressed with the introduction of Sn in $Pr_3Co_{2+x}Ge_{7-y}Sn_y$,[70] with only two metamagnetic transitions occurring at applied fields of <1 T. Both phases are far below the expected magnetization for Pr, approaching 1 μ_B/mol-Pr at 7 T and 4 K; however, the effective magnetic moment for $Pr_3Co_{2+x}Ge_{7-y}Sn_y$ (μ_{eff} = 3.81 μ_B/Pr) is above the theoretical spin only moment of Pr^{3+} (3.58 μ_B/Pr^{3+}). For comparison, $Pr_3Ni_{2-x}Sn_7$[71] has similar behavior, with a single metamagnetic transition occurring below 2 T and 2 K. With the identification of two newly synthesized members of the $Pr_{n+1}Co_nGe_{3n+1}$ series, n = 3 and n = 4, we now have a platform to demonstrate the tunability of this series for future work (Figure 1).

The n = 3 member $Pr_4Co_{3+x}Ge_{10-y}Sn_y$ (see Figure 2 for structural representation and Table S1 for crystallographic data) is isostructural to $Eu_2Ni_{2-x}Sn_5$ ($Eu_4Ni_{4-x}Sn_{10}$, *Cmcm*).[72] The atomic positions for both structures are shown in Table S2. $Pr_4Co_{3+x}Ge_{10-y}Sn_y$ can be described as a stacking of $CeNiSi_2$ alternating with two slabs of $BaNiSn_3/AuCu_3$. The main differences between the $Eu_4Ni_{4-x}Sn_{10}$ and $Pr_4Co_{3+x}Ge_{10-y}Sn_y$ structures are (1) the complexity of the disorder and (2) the relative occupancy of the transition metals in the disordered components. In $Eu_4Ni_{4-x}Sn_{10}$, the disorder is composed of two components: $AuCu_3$ and $BaNiSn_3$ in one orientation. In contrast, the $Pr_4Co_{3+x}Ge_{10-y}Sn_y$ structure is composed of three disordered components, which are $AuCu_3$ and two orientations of $BaNiSn_3$ (right side up and down relative to the b axis).

$Pr_5Co_{4+x}Ge_{13-y}Sn_y$ (Figure 3 and Tables S1 and S3) of the $Ce_5Co_4Ge_{13}$ structure type[25] can be described as a Co incorporated Nb_5Ga_{13}-type structure composed of AlB_2, $BaNiSn_3$, and $BaNiSn_3/AuCu_3$ subunits. The use of AlB_2 subunits is analogous to $CeNiSi_2$, resulting in a stacking pattern of three $BaNiSn_3/AuCu_3$ subunits separated by one $CeNiSi_2$ subunit. In the report of $Ce_5Co_4Ge_{13}$, a disordered model with $BaNiSn_3/AuCu_3$ subunits was suggested, as a logical explanation of the observed residual electron densities. This disorder is also observed in the published structure of $Ce_5Co_{4+x}Ge_{13-y}Sn_y$[26] and in the model of $Pr_5Co_{4+x}Ge_{13-y}Sn_y$ presented in this manuscript. Like $Pr_4Co_{3+x}Ge_{10-y}Sn_y$, there are also reduced Co occupancies relative to the Ge occupancies within the disordered components.

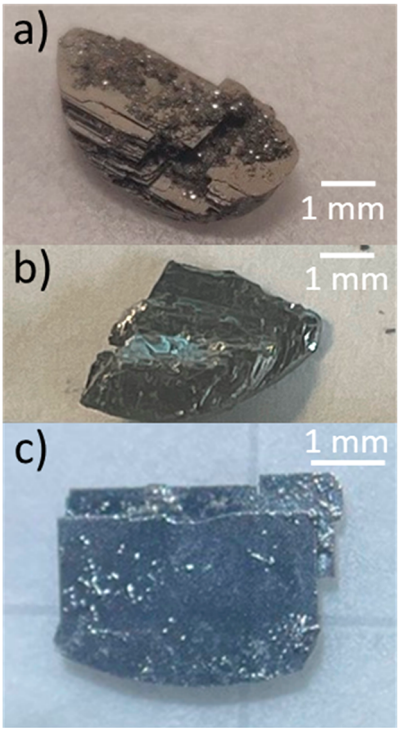

Figure 1. (a) Aggregate crystals containing $Pr_5Co_{4+x}Ge_{13-y}Sn_y$ before etching and (b) a fragment after etching. (c) Plates of $Pr_4Co_{3+x}Ge_{10-y}Sn_y$.

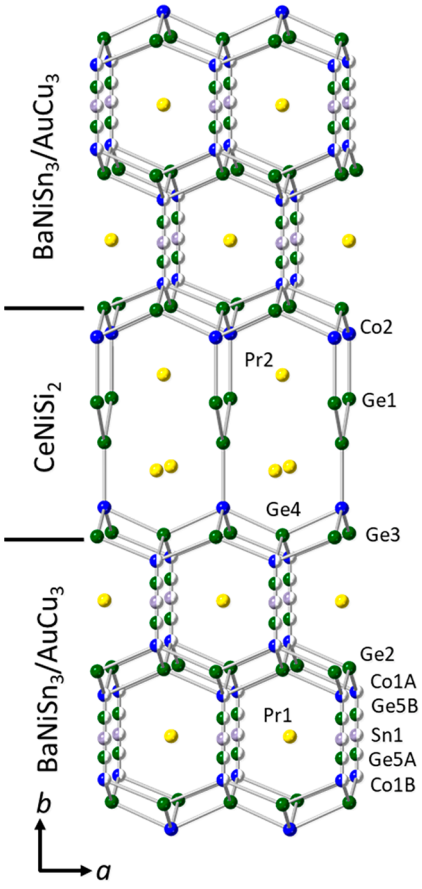

Figure 2. Crystal structure of $Pr_4Co_{3+x}Ge_{10-y}Sn_y$, where yellow, blue, green, and gray spheres represent Pr, Co, Ge, and Sn, respectively.

https://doi.org/10.1021/acsomega.2c02152
ACS Omega 2022, 7, 19048−19057

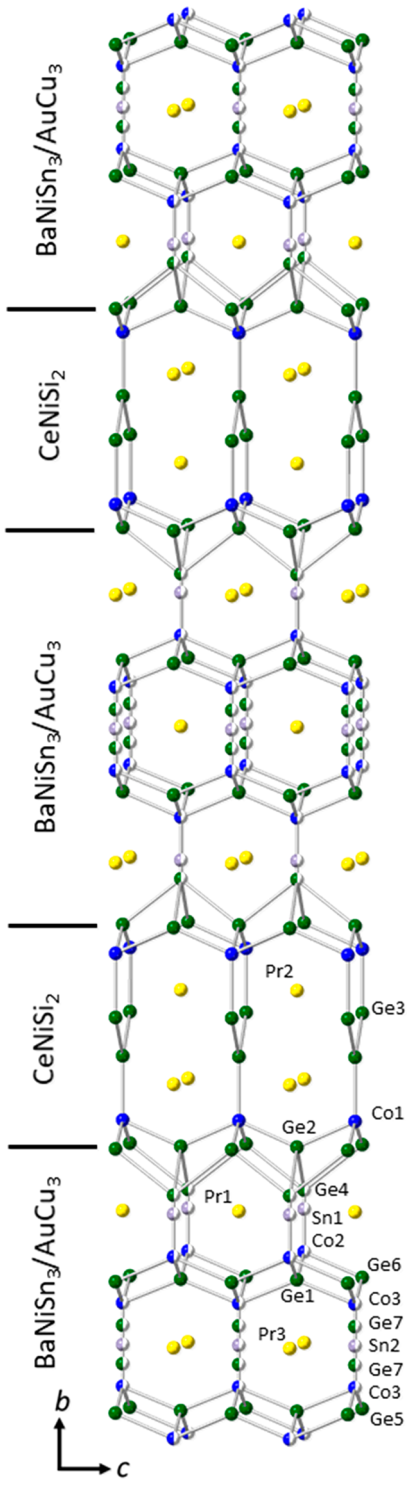

Figure 3. Crystal structure of $Pr_5Co_{4+x}Ge_{13-y}Sn_y$, where yellow, blue, green, and gray spheres represent Pr, Co, Ge, and Sn, respectively.

4. CHALLENGES AND FUTURE OUTLOOK

While single crystal diffraction provides great insights into the crystal structure, it is imperative to know if the single crystal is truly representative of the entire batch of crystals grown. With powder diffraction, the experiment can confirm the purity and homogeneity of the crystalline sample. For $Pr_4Co_{3+x}Ge_{10-y}Sn_y$, while the structural models obtained through single crystal X-ray diffraction are in good agreement with measured intensities, significant differences arise when compared to the bulk sample, revealing the challenges of using coherent scattering methods to model disorder. The local environment of the Pr1 site has, based on single crystal models, five potential configurations over a length of approximately 5 Å which extends diffraction techniques to the limits of their capabilities when considering the similar X-ray scattering cross sections of Co and Ge, the similar contact distances seen in the literature from Co−Co, Co−Ge, and Ge−Ge contacts depending on the covalency, and the similar bonding behaviors of Sn and Ge. Thus, despite the acceptable refinement statistics and reasonable crystal chemistry of the $Pr_4Co_{3+x}Ge_{10-y}Sn_y$ model obtained from single crystal diffraction, the model must be refined further. While in many circumstances single crystal X-ray and powder diffraction are satisfactory to obtain exceptional models of disordered crystal structures,[73] for the future of quantum materials, drawing attention to the use of complementary structure techniques for their characterization is extremely important. The electronic contributions of minor structural defects can result in significant differences in physical properties. The structural investigations of heavy fermion compound Ce_2RhIn_8 are a model learning tool in how complementary structure techniques come together.[74] Incongruencies in Bragg peak intensities observed in X-ray powder diffraction inspired electron diffraction experiments ultimately leading to high-resolution synchrotron X-ray reciprocal space mapping of single crystals and high-resolution neutron powder diffraction experiments that identified unexpected two-phase mosaic disorder in a crystal structure otherwise believed to be ordered. The identification of complex disorder in Ce_2RhIn_8 went on to be used to rationalize the physical properties of other related heavy electron materials[75−78] and inspire more detailed synthetic investigations,[79] again underscoring the importance of thorough structural characterization.

A similar approach could be used for the $Pr_{n+1}Co_nGe_{3n+1}$ homologous series to clarify the number of apparent disorder configurations in the $BaNiSn_3/AuCu_3$-type subunits through short-range correlations, address the peak broadening of the (2 0 0) and (0 0 2) reflections, and identify the cause of non-Bragg scattering at the 10° to 11° 2θ range using long-range correlations. Techniques such as pair distribution function, neutron diffraction methods, electron microscopy, and electron diffraction methods provide alternative views of a material that, taken together, work to elucidate the structure of compounds from local disorder at specific atomic sites to macroscopic disorder such as stacking faults and mosaicity effects.

We have successfully synthesized two members of the $Pr_{n+1}Co_nGe_{3n+1}$ homologous series: $Pr_4Co_{3+x}Ge_{10-y}Sn_y$ and $Pr_5Co_{4+x}Ge_{13-y}Sn_y$. However, phase pure synthesis of a single homologous series member remains a significant challenge. Due to the similar stoichiometries based on the relative elemental ratios of the $Pr_{n+1}Co_nGe_{3n+1}$ series members, altering the reactant ratios proved ineffective. As such, our remaining option has been to refine the temperature profile, but without comprehensive ternary or quaternary phase diagrams, there is little guidance for this approach. Unexpectedly, raising the Sn concentration of the reaction has been the most successful method of obtaining phase pure homologous series members, despite producing the byproduct $Pr_2Co_3Ge_5$. This is similar to recent findings regarding Y_4RuGe_8.[80] The possibility of altering the flux concentration to isolate different n members presents a promising new method of reaction tuning that has inspired an investigation into in situ X-ray powder diffraction methods[81−83] and thermal analysis[84,85] to understand how changing flux

https://doi.org/10.1021/acsomega.2c02152
ACS Omega 2022, 7, 19048−19057

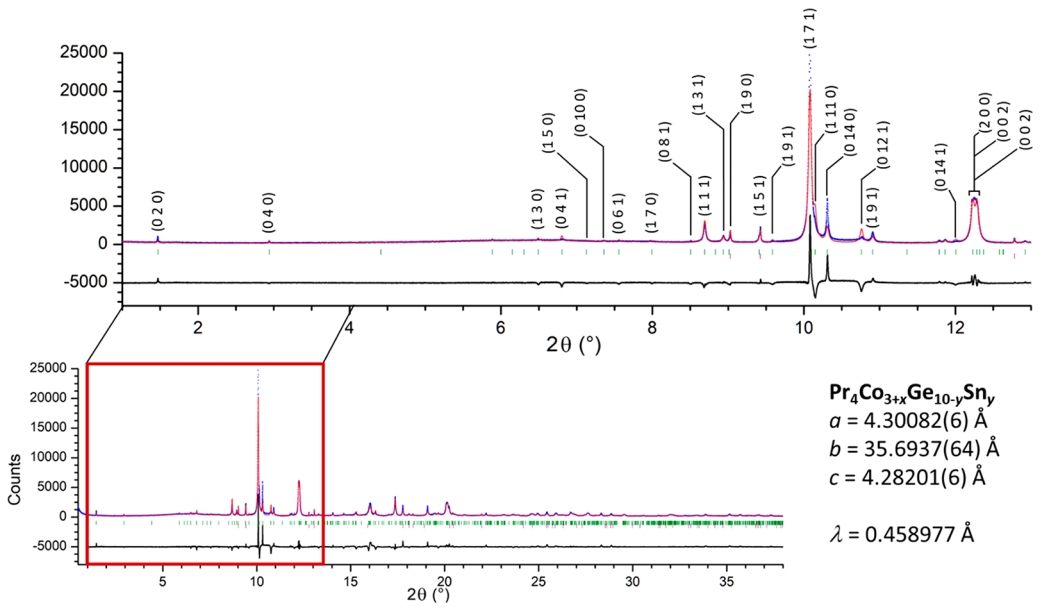

Figure 4. High-resolution synchrotron X-ray powder diffraction collected at 11-BM at the Advanced Photon Source of $Pr_4Co_{3+x}Ge_{10-y}Sn_y$ shown in blue (λ = 0.458977 Å). The calculated fit from Rietveld refinement is shown in red, with the difference plot shown in black. Green and purple tick marks indicate $Pr_4Co_{3+x}Ge_{10-y}Sn_y$ and Sn reflections, respectively. Labeled reflections are those with mismatched intensities.

conditions influence the formation of homologous series members and other related phases.[86,87]

Despite these structural challenges, the $Pr_{n+1}Co_nGe_{3n+1}$ series presents new opportunities for $4f^2$ electron systems. Uncovering potential correlative effects between different crystallographic Pr sites, dimensionality, and local environment could impact local $4f$ hybridization with conduction electrons. Thus, there is strong motivation to measure the physical properties of the $Pr_{n+1}Co_nGe_{3n+1}$ homologous series. Due diligence in developing new structural models of quantum materials is equally as important to the quantum community as their physical properties. We keep these considerations in mind for the synthesis of the $Pr_{n+1}Co_nGe_{3n+1}$ homologous series, as understanding the Pr local environment is extremely important to relating crystal electric field to electronic and magnetic behavior at the intersection of topological materials and highly correlated electron systems.

5. METHODS

5.1. Synthesis. $Pr_4Co_{3+x}Ge_{10-y}Sn_y$ and $Pr_5Co_{4+x}Ge_{13-y}Sn_y$ were prepared using the flux growth method with tin as a metallic flux. The elements were combined in the ratio 3 Pr:2 Co:7 Ge:50 Sn and 3 Pr:2 Co:7 Ge:20 Sn, respectively, with the weight of the $Pr_4Co_{3+x}Ge_{10-y}Sn_y$ reactants being 0.50 g, Sn flux 2.80 g $Pr_5Co_{4+x}Ge_{13-y}Sn_y$ reactants' weight 0.25 g, and Sn flux 0.56 g. The elements were transferred to an alumina Canfield crucible[88] and sealed in fused silica tubes under ~1/3 atm of Ar gas. The $Pr_5Co_{4+x}Ge_{13-y}Sn_y$ ampule was placed in a programmable furnace at 300 °C and heated to 1175 °C at the rate 100 °C/h. The sample dwelled at 1175 °C for 24 h and was cooled to 815 °C at the rate 3 °C/h, where it dwelled for approximately 6 h before removal and centrifugation of excess Sn flux. Residual flux was removed via etching in dilute HCl. A layered aggregate of plates, approximately 2 mm × 4 mm × 7 mm in size, composed of $Pr_3Co_{2+x}Ge_{7-y}Sn_y$, $Pr_4Co_{3+x}Ge_{10-y}Sn_y$, and $Pr_5Co_{4+x}Ge_{13-y}Sn_y$ was obtained. The $Pr_4Co_{3+x}Ge_{10-y}Sn_y$ reaction followed similar parameters with a 4 h dwell time at 1175 °C and a 30 h dwell time at 815 °C. One large platelike crystal of $Pr_4Co_{3+x}Ge_{10-y}Sn_y$, 1 mm × 3 mm × 4 mm in size, and some polyhedral shaped crystals of $Pr_2Co_3Ge_5$, approximately 1 mm × 2 mm × 2 mm in size, were obtained. Single crystals of $Pr_4Co_{3+x}Ge_{10-y}Sn_y$ and $Pr_5Co_{4+x}Ge_{13-y}Sn_y$ were cut from their respective samples. The $Pr_4Co_{3+x}Ge_{10-y}Sn_y$ method was reproduced with a modified temperature profile for comparison to the synthesis of $Pr_5Co_{4+x}Ge_{13-y}Sn_y$, where the dwell time at 1175 °C was increased to 24 h, and the sample was removed from the furnace upon reaching 815 °C with less than 1 h of dwell time. From this sample, $Pr_2Co_3Ge_5$ was obtained as a dominant product. Small platelike crystals below 1 mm × 1 mm × 1 mm in size were also observed.

5.2. Laboratory Powder X-ray Diffraction. Powder X-ray diffraction data was collected on an aggregate containing $Pr_3Co_{2+x}Ge_{7-y}Sn_y$, $Pr_4Co_{3+x}Ge_{10-y}Sn_y$, and $Pr_5Co_{4+x}Ge_{13-y}Sn_y$ using a Bruker D8 Advance diffractometer operating at 40 kV/30 mA with Cu Kα radiation (λ = 1.54184 Å) equipped with a LYNXEYE detector. Data was collected in the 2θ range from 5.0° to 90°. Laboratory powder X-ray diffraction was performed on the aggregate sample that was used to collect $Pr_5Co_{4+x}Ge_{13-y}Sn_y$ single crystal data, and it was determined that the sample contained an intergrown mixture of series members; however, the presence of more than a single n member made accurate phase identification extremely difficult due to overlapping Bragg reflections and air scattering present in the laboratory powder diffraction. To overcome this problem, high-resolution powder diffraction data was collected at beamline 11-BM at the Advanced Photon Source of Argonne National Laboratory, where a combination of using a transmission mode, analyzer crystals, and high photon flux resulted in far higher signal-to-noise ratios.

5.3. High-Resolution Powder X-ray Diffraction. High-resolution powder X-ray diffraction data (λ = 0.458977 Å) was collected in the 2θ range from 0.5° to 43.5° for $Pr_5Co_{4+x}Ge_{13-y}Sn_y$ and from 0.5° to 48.8° for $Pr_4Co_{3+x}Ge_{10-y}Sn_y$ at the 11-BM beamline at the Advanced Photon Source of Argonne National Laboratory. All data modeling was carried out using TOPAS-Academic software. A two-phase Rietveld refine-

https://doi.org/10.1021/acsomega.2c02152
ACS Omega 2022, 7, 19048−19057

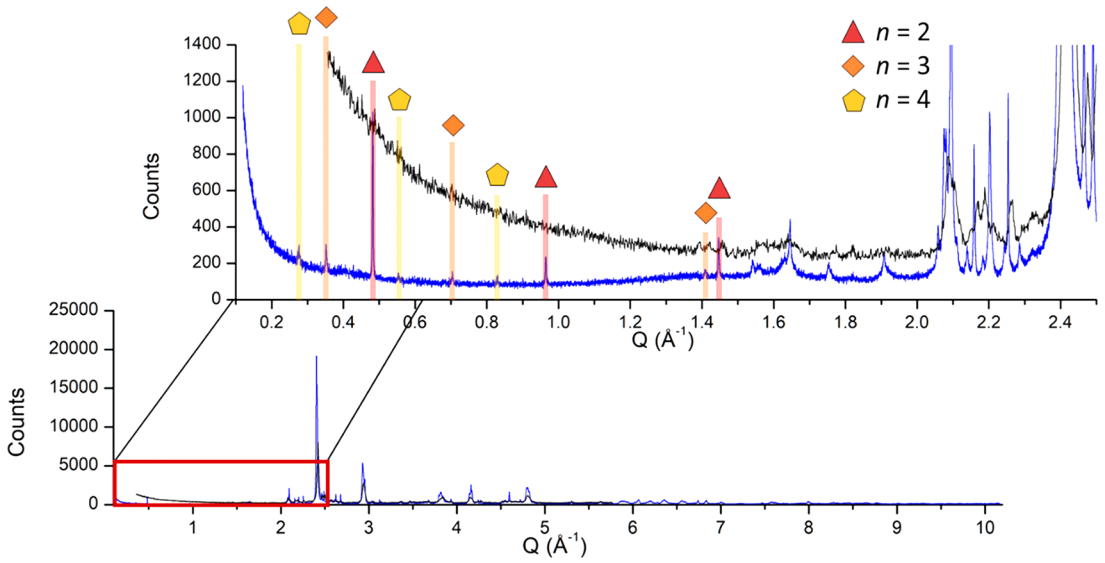

Figure 5. Comparison of laboratory (black, λ = 1.5406 Å) and high-resolution synchrotron (blue, λ = 0.458977 Å) X-ray powder diffraction data taken at 11-BM at the Advanced Photon Source. Colored lines and shapes indicate the (0 2n 0) reflections used to identify members of the homologous series $Pr_3Co_{2+x}Ge_{7-y}Sn_y$ (blue triangle), $Pr_4Co_{3+x}Ge_{10-y}Sn_y$ (yellow diamond), and $Pr_5Co_{4+x}Ge_{13-y}Sn_y$ (red pentagon).

Table 1. Lattice Parameters Obtained from the Pawley Refinement of $Pr_5Co_{4+x}Ge_{13-y}Sn_y$

	Space Group	a (Å)	b (Å)	c (Å)	V (Å^3)
$Pr_3Co_{2+x}Ge_{7-y}Sn_y$	*Cmmm*	4.25340(3)	26.0705(20)	4.29152(3)	475.881(7)
$Pr_4Co_{3+x}Ge_{10-y}Sn_y$	*Cmcm*	4.36710(14)	35.6931(63)	4.20920(14)	656.113(34)
$Pr_5Co_{4+x}Ge_{13-y}Sn_y$	*Cmmm*	4.28048(5)	45.4234(67)	4.30056(7)	836.175(21)

ment using data collected on a ground fragment of the single phase plate of $Pr_4Co_{3+x}Ge_{10-y}Sn_y$ and Sn (Figure 4) was able to account for all visible Bragg reflections, showing the sample is phase pure. However, mismatched intensities and non-Bragg scattering reveal a more complex story than captured through single crystal methods. The intensities of the (0 2 0), (1 7 1), (1 11 0), and (0 14 0) reflections are different than the calculated model. Given the platelike morphology of crystals grown from this series and the large anisotropy of the lattice parameters, intensity corrections were attempted by considering the preferred orientation of different combinations of the following reflection families: (0 2n 0), (1 2n−1 0), (0 2n−1 1), and (1 2n−1 1), but the improvements on the refinement were insignificant. Anisotropic strain broadening was also evaluated with little improvement to the refinement. As all mismatched intensities have dependence on the b crystallographic direction, attempts were made to alter the disorder model obtained through single crystal diffraction. While the intensities were improved considerably, the resulting structural model disagreed with the compositions obtained from elemental analysis and single crystal models.

One factor that could be impacting the accuracy of the single crystal structure refinement is the lack of visibility for the (0 2 0) reflection. Due to the large b axis of $Pr_4Co_{3+x}Ge_{10-y}Sn_y$, the (0 2 0) reflection appears at a low 2θ angle of 4.56° (Mo Kα, λ = 0.71073 Å). This is outside the 2θ collection range 10.06° to 59.74° due to shadowing from the beam stop either fully or partially blocking this reflection. Since the disorder is strongly correlated to the (0 2n 0) reflections, the (0 2 0) reflection is particularly sensitive to changes in the structural model. Without this reflection, the single crystal model lacks key intensity information against which to refine the structural model. This is an additional challenge when working with compounds with very large unit cells, especially when blocked reflections are critical to regions of disorder. Due to the mixed phase nature of the sample containing $Pr_5Co_{4+x}Ge_{13-y}Sn_y$, a Pawley refinement was performed. From this data, low-angle (0 2n 0) reflections were visible (Figure 5), which were critical in identifying the members of the $Pr_{n+1}Co_nGe_{3n+1}$ series due to their strong correlation with the systematically elongated b axis of the series. Yet, without a single phase sample we were limited in our ability to refine the crystal structure against the bulk powder diffraction pattern through Rietveld refinement. Instead, a Pawley refinement revealed a mixed phase system of n = 2, 3, and 4 (Table 1). Although the lattice parameters obtained for $Pr_3Co_{2+x}Ge_{7-y}Sn_y$ and $Pr_5Co_{4+x}Ge_{13-y}Sn_y$ agree with single crystal data,[70] overlapping Bragg reflections remain a challenge with clear deviations in the refined a and c lattice parameters of $Pr_4Co_{3+x}Ge_{10-y}Sn_y$ from single crystal data and phase pure powder diffraction. From here, obtaining phase pure samples will be the only way to validate the homogeneity of the disorder observed in the single crystal model for $Pr_5Co_{4+x}Ge_{13-y}Sn_y$.

5.4. Single Crystal X-ray Diffraction. Single crystal X-ray diffraction data was obtained at room temperature using a Bruker D8 Quest Kappa single crystal X-ray diffractometer, equipped with an IμS microfocus source (Mo Kα, λ = 0.71073 Å), HELIOS optics monochromator, and PHOTON II CPAD detector. The Bruker SAINT program was used to integrate the diffraction data, and the intensities were corrected for absorption via a multiscan method implemented in SADABS 2016/2.[89] Preliminary starting models were generated using the intrinsic phasing methods in SHELXT[90] and subsequently anisotropically refined (full-matrix least-squares on F^2) using SHELXL.[91] Details of both structure refinements can be found in Tables S1−S3. Single crystals of $Pr_4Co_{3+x}Ge_{10-y}Sn_y$ (0.01 mm × 0.01 mm × 0.02 mm) and $Pr_5Co_{4+x}Ge_{13-y}Sn_y$ (0.02 mm ×

https://doi.org/10.1021/acsomega.2c02152
ACS Omega 2022, 7, 19048−19057

0.12 mm × 0.14 mm) were cut from their respective samples and mounted on glass fibers using two-part epoxy.

The crystal structure of $Pr_4Co_{3+x}Ge_{10-y}Sn_y$ was preliminarily modeled in the noncentrosymmetric space group *Amm*2. However, additional symmetries were detected using the ADDSYM function in PLATON, resulting in the final selection of the centrosymmetric space group *Cmcm*, in agreement with the $Eu_4Co_{4-x}Sn_{10}$ structure type. In contrast to the $Eu_4Co_{4-x}Sn_{10}$ structure type, additional electron densities of 5.43 $e^-/Å^3$ and 4.53 $e^-/Å^3$ were observed in the Pr1 local environment at (0 0.6408 0) and (0 0.7082 0), respectively. To address the observed intensities, an additional Co1B−Ge1B dimer was added. In accordance with the elemental analysis results indicating the presence of Sn incorporation, the Sn1 site was considered, leading to marginally improved refinement statistics relative to the assignment of a Ge atom. Additionally, when compared to the lattice parameters of $Pr_4Co_{3+x}Ge_{10}$ grown in In flux (a = 4.2831(7) Å, b = 35.497(8) Å, c = 4.2533(10) Å), there is a difference in the b lattice parameter of approximately 0.3 Å corresponding to the incorporation of Sn. This effect was observed in $Pr_3Co_{2+x}Ge_{7-y}Sn_y$ and $Pr_3Co_{2+x}Ge_7$ as well. The Sn incorporation in the presence of Sn flux agrees with observations from $Ce_{n+1}Co_nGe_{3n+1-y}Sn_y$ (n = 4, 5, and 6). At this point in the refinement, Co vacancies had not been considered, but a hole of −5.46 $e^-/Å^3$ was observed on the Co1A site. Thus, the Co1A, Co1B, and Co2 site occupancies were allowed to refine freely, resulting in a reduction in occupancy from ∼66% to ∼58% for Co1A, from ∼7.8% to ∼5.0% for Co1B, and from unity to 99% for Co2. The corresponding Ge sites' occupancy saw an increase from ∼66% to ∼67% for Ge1A and from ∼7.8% to ∼8.4% for Ge1B. The fully occupied Co2 site and vacancies on the Co1A and Co1B sites agree with the crystal structure determination of $Eu_4Ni_{4-x}Sn_{10}$.

The crystal structure of $Pr_5Co_{4+x}Ge_{13-y}Sn_y$ was found to crystallize in the orthorhombic space group *Cmmm*. The disorder modeled in this structure is in extremely good agreement with the refinement of $Ce_5Co_{4+x}Ge_{13-y}Sn_y$, with the Pr1 local environment consisting of one Co2−Ge4 dimer representing the $BaNiSn_3$ structure type complemented by the Sn1 site representing the $AuCu_3$ structure type and the Pr3 local environment consisting of two complementary Co3−Ge7 dimers with the Sn2 site occupying the remainder of the configurations. Unlike $Ce_5Co_{4+x}Ge_{13-y}Sn_y$, upon refining the weighting scheme, a negative electron density of −6.00 $e^-/Å^3$ was observed on the Co3 site in the Pr3 local environment. To address this, the Co3 occupancy was allowed to refine freely, where its occupancy reduced from ∼35% to ∼28%. From here, the occupancies of Co1 of the Pr2 local environment and Co2 of the Pr1 local environment were refined freely, resulting in an occupancy of approximately 99% for Co1 and a reduction the Co2 occupancy from ∼87% to ∼83%. The Co1 occupancy was fixed to unity, but the Co2 and Co3 vacancies were retained. The freely refined Co2 and Co3 sites resulted in an occupancy increase from 87% to 88% for Ge4 and from 35% to 37% for Ge7.

5.5. Elemental Analysis. Single crystals of $Pr_4Co_3Ge_{10-y}Sn_y$ and $Pr_5Co_4Ge_{13-y}Sn_y$ were analyzed using energy dispersive (X-ray) spectroscopy on a VERSA 3D focused ion beam scanning electron microscope with an acceleration voltage of 20 kV. The weight percentages obtained from EDS (normalized to Pr) resulted in the atomic formulas $Pr_{4.00(2)}Co_{3.22(1)}Ge_{9.34(7)}Sn_{0.66(1)}$ and $Pr_{5.00(3)}Co_{4.38(1)}Ge_{12.27(5)}Sn_{0.44(2)}$, which are comparable to the single crystal refinement formulas $Pr_4Co_{3.25(3)}Ge_{9.50(1)}Sn_{0.469(4)}$ and $Pr_5Co_{4.22(2)}Ge_{12.48(1)}Sn_{0.519(7)}$, respectively.

■ ASSOCIATED CONTENT

Supporting Information

The Supporting Information is available free of charge at https://pubs.acs.org/doi/10.1021/acsomega.2c02152.

Additional details on the disorder model of $Pr_4Co_{3+x}Ge_{10-y}Sn_y$ and $Pr_5Co_{4+x}Ge_{13-y}Sn_y$, the full structure refinement details of $Pr_4Co_{3+x}Ge_{10-y}Sn_y$ and $Pr_5Co_{4+x}Ge_{13-y}Sn_y$ (Table S1), a comparison of atomic positions for $Pr_4Co_{3+x}Ge_{10-y}Sn_y$ and $Eu_4Ni_{4-x}Sn_{10}$ (Table S2), and a comparison of atomic positions for $Pr_5Co_4Ge_{13-y}Sn_y$ and $Ce_5Co_{4+x}Ge_{13-y}Sn_y$ (Table S3) (PDF)

CIF data for $Pr_4Co_{3+x}Ge_{10-y}Sn_y$ (CIF)

CIF data for $Pr_5Co_{4+x}Ge_{13-y}Sn_y$(CIF)

■ AUTHOR INFORMATION

Corresponding Author

Julia Y. Chan − *Department of Chemistry & Biochemistry, Baylor University, Waco, Texas 76798, United States;* orcid.org/0000-0003-4434-2160; Email: julia_chan@baylor.edu

Authors

Trent M. Kyrk − *Department of Chemistry & Biochemistry, Baylor University, Waco, Texas 76798, United States*

Moises Bravo − *Department of Chemistry & Biochemistry, Baylor University, Waco, Texas 76798, United States;* orcid.org/0000-0002-1846-4618

Gregory T. McCandless − *Department of Chemistry & Biochemistry, Baylor University, Waco, Texas 76798, United States*

Saul H. Lapidus − *X-ray Science Division, Advanced Photon Source, Argonne National Laboratory, Argonne, Illinois 60439, United States;* orcid.org/0000-0002-7486-4325

Complete contact information is available at: https://pubs.acs.org/10.1021/acsomega.2c02152

Notes

The authors declare no competing financial interest.

■ ACKNOWLEDGMENTS

This material is based upon work supported by the U.S. Department of Energy, Office of Science, Office of Workforce Development for Teachers and Scientists, Office of Science Graduate Student Research (SCGSR) program. The SCGSR program is administered by the Oak Ridge Institute for Science and Education for the DOE under contract number DE−SC0014664. J.Y.C. gratefully acknowledges the support of the National Science Foundation (Grant No. DMR-2209804), the Welch Foundation (Grant No. AT-2056-20210327), and the Department of Energy Grant (No. DE-SC0022068). This research used resources of the Advanced Photon Source, a U.S. Department of Energy (DOE) Office of Science user facility operated for the DOE Office of Science by Argonne National Laboratory under Contract No. DE-AC02-06CH11357.

■ REFERENCES

(1) The Rise of Quantum Materials. *Nat. Phys.* **2016**, *12*, 105−105.

(2) Ball, P. Quantum Materials: Where Many Paths Meet. *MRS Bull.* **2017**, *42*, 698−705.
(3) Broholm, C.; Fisher, I.; Moore, J.; Murnane, M.; Moreo, A.; Tranquada, J.; Basov, D.; Freericks, J.; Aronson, M.; MacDonald, A.; Fradkin, E.; Yacoby, A.; Samarth, N.; Stemmer, S.; Horton, L.; Horwitz, J.; Davenport, J.; Graf, M.; Krause, J.; Pechan, M.; Perry, K.; Rhyne, J.; Schwartz, A.; Thiyagarajan, T.; Yarris, L.; Runkles, K. *Basic Research Needs Workshop on Quantum Materials for Energy Relevant Technology*; USDOE Office of Science (SC), Basic Energy Sciences (BES): United States, 2016-02-10, 2016.
(4) Moore, J. E. The Birth of Topological Insulators. *Nature* **2010**, *464*, 194−198.
(5) Giustino, F.; Lee, J. H.; Trier, F.; Bibes, M.; Winter, S. M.; Valentí, R.; Son, Y.-W.; Taillefer, L.; Heil, C.; Figueroa, A. I.; Plaçais, B.; Wu, Q.; Yazyev, O. V.; Bakkers, E. P. A. M.; Nygård, J.; Forn-Díaz, P.; De Franceschi, S.; McIver, J. W.; Torres, L. E. F. F.; Low, T.; Kumar, A.; Galceran, R.; Valenzuela, S. O.; Costache, M. V.; Manchon, A.; Kim, E.-A.; Schleder, G. R.; Fazzio, A.; Roche, S. The 2021 Quantum Materials Roadmap. *J. Phys. Mater.* **2020**, *3*, 042006.
(6) Yan, B.; Felser, C. Topological Materials: Weyl Semimetals. *Annu. Rev. Condens. Matter Phys.* **2017**, *8*, 337−354.
(7) Lai, H.-H.; Grefe, S. E.; Paschen, S.; Si, Q. Weyl-Kondo Semimetal in Heavy-Fermion Systems. *Proc. Natl. Acad. Sci. U.S.A.* **2018**, *115*, 93−97.
(8) Tokura, Y.; Kanazawa, N. Magnetic Skyrmion Materials. *Chem. Rev.* **2021**, *121*, 2857−2897.
(9) Alfieri, A.; Anantharaman, S. B.; Zhang, H.; Jariwala, D. Nanomaterials for Quantum Information Science and Engineering. *Adv. Mater.* **2022**, 2109621.
(10) Si, Q.; Steglich, F. Heavy Fermions and Quantum Phase Transitions. *Science* **2010**, *329*, 1161−1166.
(11) Wirth, S.; Steglich, F. Exploring Heavy Fermions from Macroscopic to Microscopic Length Scales. *Nat. Rev. Mater.* **2016**, *1*, 16051.
(12) Grin, Y. N.; Yarmolyuk, Y. P.; Gladyshevskij, E. I. Crystal structures of R_2CoGa_8 compounds (R = Sm, Gd, Tb, Dy, Ho, Er, Tm, Lu, Y) and $RCoGa_5$ compounds (R = Gd, Tb, Dy, Ho, Er, Tm, Lu, Y). *Kristallografiya* **1979**, *24*, 242−246.
(13) Thompson, J. D.; Movshovich, R.; Fisk, Z.; Bouquet, F.; Curro, N. J.; Fisher, R. A.; Hammel, P. C.; Hegger, H.; Hundley, M. F.; Jaime, M.; Pagliuso, P. G.; Petrovic, C.; Phillips, N. E.; Sarrao, J. L. Superconductivity and Magnetism in a New Class of Heavy-Fermion Materials. *J. Magn. Magn. Mater.* **2001**, *226*−*230*, 5−10.
(14) Latturner, S. E.; Kanatzidis, M. G. $RE(AuAl_2)_nAl_2(Au_xSi_{1-x})_2$: A New Homologous Series of Quaternary Intermetallics Grown from Aluminum Flux. *Inorg. Chem.* **2008**, *47*, 2089−2097.
(15) Tursina, A.; Khamitcaeva, E.; Gribanov, A.; Gnida, D.; Kaczorowski, D. $CePd_2Al_2$, $CePd_3Al_3$, and $CePd_4Al_4$—A New Homologous Series Built of $CaBe_2Ge_2$- and CsCl-type Units. *Inorg. Chem.* **2015**, *54*, 3439−3445.
(16) Guo, S.-P.; You, T.-S.; Bobev, S. Closely Related Rare-Earth Metal Germanides $RE_2Li_2Ge_3$ and $RE_3Li_4Ge_4$ (RE = La-Nd, Sm): Synthesis, Crystal Chemistry, and Magnetic Properties. *Inorg. Chem.* **2012**, *51*, 3119−3129.
(17) Guo, S.-P.; You, T.-S.; Jung, Y.-H.; Bobev, S. Synthesis, Crystal Chemistry, and Magnetic Properties of $RE_7Li_8Ge_{10}$ and $RE_{11}Li_12Ge_{16}$ (RE = La-Nd, Sm): New Members of the $[REGe_2]_n[RELi_2Ge]_m$ Homologous Series. *Inorg. Chem.* **2012**, *51*, 6821−6829.
(18) Lin, X.; Tabassum, D.; Mar, A. Narrowing The Gap: From Semiconductor to Semimetal in The Homologous Series of Rare-Earth Zinc Arsenides $RE_{2-y}Zn_4As_4{\cdot}n(REAs)$ and Mn-Substituted Derivatives $RE_{2-y}Mn_xZn_{4-x}As_4{\cdot}n(REAs)$ (RE = La-Nd, Sm, Gd). *Dalton Trans.* **2015**, *44*, 20254−20264.
(19) Mathur, N. D.; Grosche, F. M.; Julian, S. R.; Walker, I. R.; Freye, D. M.; Haselwimmer, R. K. W.; Lonzarich, G. G. Magnetically Mediated Superconductivity in Heavy Fermion Compounds. *Nature* **1998**, *394*, 39−43.
(20) Park, T.; Ronning, F.; Yuan, H. Q.; Salamon, M. B.; Movshovich, R.; Sarrao, J. L.; Thompson, J. D. Hidden Magnetism and Quantum Criticality in the Heavy Fermion Superconductor $CeRhIn_5$. *Nature* **2006**, *440*, 65−68.
(21) Hegger, H.; Petrovic, C.; Moshopoulou, E. G.; Hundley, M. F.; Sarrao, J. L.; Fisk, Z.; Thompson, J. D. Pressure-Induced Superconductivity in Quasi-2D $CeRhIn_5$. *Phys. Rev. Lett.* **2000**, *84*, 4986−4989.
(22) Macaluso, R. T.; Sarrao, J. L.; Moreno, N. O.; Pagliuso, P. G.; Thompson, J. D.; Fronczek, F. R.; Hundley, M. F.; Malinowski, A.; Chan, J. Y. Single-Crystal Growth of Ln_2MIn_8 (Ln = La, Ce; M = Rh, Ir): Implications for the Heavy-Fermion Ground State. *Chem. Mater.* **2003**, *15*, 1394−1398.
(23) Weiland, A.; Felder, J. B.; McCandless, G. T.; Chan, J. Y. One Ce, Two Ce, Three Ce, Four? An Intermetallic Homologous Series to Explore: $A_{n+1}B_nX_{3n+1}$. *Chem. Mater.* **2020**, *32*, 1575−1580.
(24) Méot-Meyer, M.; Venturini, G.; Malaman, B.; Roques, B. De Nouveaux Isotypes Lacunaires de $CeNiSi_2$: Les Germaniures RCo_xGe_2, R = Y, La-Sm, Gd-Lu, $0 < x \leq 1$. *Mater. Res. Bull.* **1985**, *20*, 1515−1521.
(25) Belan, B.; Stępeń-damm, J.; Gladyshevskii, R.; Bodak, O. The New Structure Type $Ce_5Co_4Ge_{13}$. *Chem. Met. Alloys* **2008**, *1*, 43−48.
(26) Weiland, A.; Wei, K.; McCandless, G. T.; Baumbach, R. E.; Chan, J. Y. Fantastic n = 4: $Ce_5Co_{4+x}Ge_{13-y}Sn_y$ of the $A_{n+1}M_nX_{3n+1}$ Homologous Series. *J. Chem. Phys.* **2021**, *154*, 114707.
(27) Felder, J. B.; Weiland, A.; Hodovanets, H.; McCandless, G. T.; Estrada, T. G.; Martin, T. J.; Walker, A. V.; Paglione, J.; Chan, J. Y. Law and Disorder: Special Stacking Units—Building the Intergrowth $Ce_6Co_5Ge_{16}$. *Inorg. Chem.* **2019**, *58*, 6037−6043.
(28) Weiland, A.; Wei, K.; McCandless, G. T.; Felder, J. B.; Eddy, L. J.; Baumbach, R. E.; Chan, J. Y. Strongly Correlated Electron Behavior In a New Member of The $A_{n+1}B_nX_{3n+1}$ Homologous Series: $Ce_7Co_6Ge_{19}$. *Phys. Rev. Mater.* **2020**, *4*, 074408.
(29) Venturini, G.; Méot-Meyer, M.; Malaman, B.; Roques, B. De Nouvelles Séries de Germaniures, Isotypes de $Yb_3Rh_4Sn_{13}$ et $BaNiSn_3$, dans les Systèmes Ternaires TR T Ge où TR est un Elément des Terres Rares et T = Co, Rh, Ir, Ru, Os. *J. Less-Common Met.* **1985**, *113*, 197−204.
(30) Weng, Z.; Smidman, M.; Jiao, L.; Lu, X.; Yuan, H. Q. Multiple Quantum Phase Transitions and Superconductivity in Ce-Based Heavy Fermions. *Rep. Prog. Phys.* **2016**, *79*, 094503.
(31) Doniach, S. The Kondo Lattice and Weak Antiferromagnetism. *Physica B+C* **1977**, *91*, 231−234.
(32) Pecharsky, V. K.; Gschneidner, K. A. $CeCo_{0.89}Ge_2$: A Heavy-Fermion System. *Phys. Rev. B* **1991**, *43*, 8238−8244.
(33) Mun, E. D.; Lee, B. K.; Kwon, Y. S.; Jung, M. H. Kondo Ground State of $CeCoGe_2$ With j = 5/2. *Phys. Rev. B* **2004**, *69*, 085113.
(34) Ramachandran, B.; Chang, P. C.; Kuo, Y. K.; Lue, C. S. Electrical and Thermal Transport Properties of Intermetallic $RCoGe_2$ (R= Ce and La) Compounds. *J. Phys.: Condens. Matter* **2014**, *26*, 255601.
(35) Thamizhavel, A.; Takeuchi, T.; D Matsuda, T.; Haga, Y.; Sugiyama, K.; Settai, R.; Ōnuki, Y. Unique Magnetic Phases in an Antiferromagnet $CeCoGe_3$. *J. Phys. Soc. Jpn.* **2005**, *74*, 1858−1864.
(36) Settai, R.; Okuda, Y.; Sugitani, I.; Ōnuki, Y.; Matsuda, T. D.; Haga, Y.; Harima, H. Non-Centrosymmetric Heavy Fermion Superconductivity in $CeCoGe_3$. *Int. J. Mod. Phys. B* **2007**, *21*, 3238−3245.
(37) Frey, N. C.; Horton, M. K.; Munro, J. M.; Griffin, S. M.; Persson, K. A.; Shenoy, V. B. High-Throughput Search for Magnetic and Topological Order in Transition Metal Oxides. *Sci. Adv.* **2020**, *6*, No. eabd1076.
(38) Xu, Y.; Elcoro, L.; Song, Z.-D.; Wieder, B. J.; Vergniory, M. G.; Regnault, N.; Chen, Y.; Felser, C.; Bernevig, B. A. High-Throughput Calculations of Magnetic Topological Materials. *Nature* **2020**, *586*, 702−707.
(39) Ran, S.; Eckberg, C.; Ding, Q.-P.; Furukawa, Y.; Metz, T.; Saha, S. R.; Liu, I.-L.; Zic, M.; Kim, H.; Paglione, J.; Butch, N. P. Nearly Ferromagnetic Spin-Triplet Superconductivity. *Science* **2019**, *365*, 684−687.
(40) Ishizuka, J.; Sumita, S.; Daido, A.; Yanase, Y. Insulator-Metal Transition and Topological Superconductivity in UTe_2 from a First-Principles Calculation. *Phys. Rev. Lett.* **2019**, *123*, 217001.

https://doi.org/10.1021/acsomega.2c02152
ACS Omega 2022, 7, 19048−19057

(41) Khim, S.; Landaeta, J. F.; Banda, J.; Bannor, N.; Brando, M.; Brydon, P. M. R.; Hafner, D.; Küchler, R.; Cardoso-Gil, R.; Stockert, U.; Mackenzie, A. P.; Agterberg, D. F.; Geibel, C.; Hassinger, E. Field-induced Transition within the Superconducting Sate of $CeRh_2As_2$. *Science* **2021**, *373*, 1012−1016.
(42) Nogaki, K.; Daido, A.; Ishizuka, J.; Yanase, Y. Topological Crystalline Superconductivity in Locally Noncentrosymmetric $CeRh_2As_2$. *Phys. Rev. Res.* **2021**, *3*, L032071.
(43) Fischer, M. H.; Loder, F.; Sigrist, M. Superconductivity and Local Noncentrosymmetricity in Crystal Lattices. *Phys. Rev. B* **2011**, *84*, 184533.
(44) Yoshida, T.; Sigrist, M.; Yanase, Y. Topological Crystalline Superconductivity in Locally Noncentrosymmetric Multilayer Superconductors. *Phys. Rev. Lett.* **2015**, *115*, 027001.
(45) Grefe, S. E.; Lai, H.-H.; Paschen, S.; Si, Q. Weyl-Kondo Semimetals in Nonsymmorphic Systems. *Phys. Rev. B* **2020**, *101*, 075138.
(46) Puphal, P.; Pomjakushin, V.; Kanazawa, N.; Ukleev, V.; Gawryluk, D. J.; Ma, J.; Naamneh, M.; Plumb, N. C.; Keller, L.; Cubitt, R.; Pomjakushina, E.; White, J. S. Topological Magnetic Phase in the Candidate Weyl Semimetal CeAlGe. *Phys. Rev. Lett.* **2020**, *124*, 017202.
(47) Puphal, P.; Mielke, C.; Kumar, N.; Soh, Y.; Shang, T.; Medarde, M.; White, J. S.; Pomjakushina, E. Bulk Single-Crystal Growth of The Theoretically Predicted Magnetic Weyl Semimetals RAlGe (R = Pr, Ce). *Phys. Rev. Mater.* **2019**, *3*, 024204.
(48) Destraz, D.; Das, L.; Tsirkin, S. S.; Xu, Y.; Neupert, T.; Chang, J.; Schilling, A.; Grushin, A. G.; Kohlbrecher, J.; Keller, L.; Puphal, P.; Pomjakushina, E.; White, J. S. Magnetism and Anomalous Transport in the Weyl Semimetal PrAlGe: Possible Route to Axial Gauge Fields. *npj Quantum Mater.* **2020**, *5*, 5.
(49) Sanchez, D. S.; Chang, G.; Belopolski, I.; Lu, H.; Yin, J.-X.; Alidoust, N.; Xu, X.; Cochran, T. A.; Zhang, X.; Bian, Y.; Zhang, S. S.; Liu, Y.-Y.; Ma, J.; Bian, G.; Lin, H.; Xu, S.-Y.; Jia, S.; Hasan, M. Z. Observation of Weyl Fermions in a Magnetic Non-Centrosymmetric Crystal. *Nat. Commun.* **2020**, *11*, 3356.
(50) Meng, B.; Wu, H.; Qiu, Y.; Wang, C.; Liu, Y.; Xia, Z.; Yuan, S.; Chang, H.; Tian, Z. Large Anomalous Hall Effect in Ferromagnetic Weyl Semimetal Candidate PrAlGe. *APL Mater.* **2019**, *7*, 051110.
(51) Yang, H.-Y.; Singh, B.; Lu, B.; Huang, C.-Y.; Bahrami, F.; Chiu, W.-C.; Graf, D.; Huang, S.-M.; Wang, B.; Lin, H.; Torchinsky, D.; Bansil, A.; Tafti, F. Transition From Intrinsic to Extrinsic Anomalous Hall Effect in the Ferromagnetic Weyl Semimetal $PrAlGe_{1-x}Si_x$. *APL Mater.* **2020**, *8*, 011111.
(52) Puphal, P.; Krebber, S.; Suard, E.; Cubitt, R.; Wang, C.; Shang, T.; Ukleev, V.; White, J. S.; Pomjakushina, E. Development of Magnetism in The Solid Solution of $Ce_{1-x}Pr_xAlGe$: From Magnetic Topology to Spin Glass. *Phys. Rev. B* **2020**, *101*, 214416.
(53) Onimaru, T.; Kusunose, H. Exotic Quadrupolar Phenomena in Non-Kramers Doublet Systems — The Cases of PrT_2Zn_{20} (T = Ir, Rh) and PrT_2Al_{20} (T = V, Ti) —. *J. Phys. Soc. Jpn.* **2016**, *85*, 082002.
(54) Van Dyke, J. S.; Zhang, G.; Flint, R. Field-Induced Ferrohastatic Phase in Cubic Non-Kramers Doublet Systems. *Phys. Rev. B* **2019**, *100*, 205122.
(55) Matsubayashi, K.; Tanaka, T.; Sakai, A.; Nakatsuji, S.; Kubo, Y.; Uwatoko, Y. Pressure-Induced Heavy Fermion Superconductivity in the Nonmagnetic Quadrupolar System $PrTi_2Al_{20}$. *Phys. Rev. Lett.* **2012**, *109*, 187004.
(56) Sakai, A.; Nakatsuji, S. Kondo Effects and Multipolar Order in the Cubic $PrTr_2Al_{20}$ (Tr = Ti, V). *J. Phys. Soc. Jpn.* **2011**, *80*, 063701.
(57) Patri, A. S.; Kim, Y. B. Unconventional Superconductivity arising from Multipolar Kondo Interactions. *SciPost Phys.* **2022**, *12*, DOI: 10.21468/SciPostPhys.12.2.057
(58) Yatskar, A.; Beyermann, W. P.; Movshovich, R.; Canfield, P. C.; Panchula, A.; Bud'ko, S. L. Unexpected Heavy-Electron Behavior at Low Temperatures in $PrInAg_2$. *Phys. B: Condens. Matter* **1997**, *230*−*232*, 46−48.
(59) Yatskar, A.; Beyermann, W. P.; Movshovich, R.; Canfield, P. C. Possible Correlated-Electron Behavior from Quadrupolar Fluctuations in $PrInAg_2$. *Phys. Rev. Lett.* **1996**, *77*, 3637−3640.
(60) Onimaru, T.; Matsumoto, K. T.; Inoue, Y. F.; Umeo, K.; Sakakibara, T.; Karaki, Y.; Kubota, M.; Takabatake, T. Antiferroquadrupolar Ordering in a Pr-Based Superconductor $PrIr_2Zn_{20}$. *Phys. Rev. Lett.* **2011**, *106*, 177001.
(61) Onimaru, T.; Nagasawa, N.; Matsumoto, K. T.; Wakiya, K.; Umeo, K.; Kittaka, S.; Sakakibara, T.; Matsushita, Y.; Takabatake, T. Simultaneous Superconducting and Antiferroquadrupolar Transitions in $PrRh_2Zn_{20}$. *Phys. Rev. B* **2012**, *86*, 184426.
(62) Yanagisawa, T.; Hidaka, H.; Amitsuka, H.; Nakamura, S.; Awaji, S.; Green, E. L.; Zherlitsyn, S.; Wosnitza, J.; Yazici, D.; White, B. D.; Maple, M. B. Quadrupolar Susceptibility and Magnetic Phase Diagram of $PrNi_2Cd_{20}$ with Non-Kramers Doublet Ground State. *Philos. Mag.* **2020**, *100*, 1268−1281.
(63) Das, P. K.; Bhattacharyya, A.; Kulkarni, R.; Dhar, S. K.; Thamizhavel, A. Anisotropic Magnetic Properties and Giant Magnetocaloric Effect of Single-Crystal PrSi. *Phys. Rev. B* **2014**, *89*, 134418.
(64) Anand, V. K.; Hossain, Z.; Geibel, C. Magnetic Order in $Pr_2Pd_3Ge_5$ and Possible Heavy-Fermion Behavior in $Pr_2Rh_3Ge_5$. *Phys. Rev. B* **2008**, *77*, 184407.
(65) Wang, Z.; Zhao, H.; Lyu, M.; Xiang, J.; Isikawa, Y.; Zhang, S.; Sun, P. Frustrated Antiferromagnetism and Heavy-Fermion-Like Behavior in PrPdAl. *Phys. Rev. B* **2022**, *105*, 125113.
(66) Nair, H. S.; Ogunbunmi, M. O.; Ghosh, S. K.; Adroja, D. T.; Koza, M. M.; Guidi, T.; Strydom, A. M. Absence of a Long-Range Ordered Magnetic Ground State in $Pr_3Rh_4Sn_{13}$ Studied Through Specific Heat and Inelastic Neutron Scattering. *J. Phys.: Condens. Matter* **2018**, *30*, 145601.
(67) Patil, N. G.; Ramakrishnan, S. Magnetism In The $R_5T_4Sn_{10}$ (R = Ce, Pr, and Nd; T = Rh and Ir) system. *Phys. Rev. B* **1997**, *56*, 3360−3371.
(68) Ramakrishnan, S.; Mydosh, J. A. Multiple Phase Transitions in Rare Earth $R_5T_4M_{10}$ (T = Rh, Ir and M = Si, Ge, Sn). *J. Magn. Magn. Mater.* **2007**, *310*, 207−213.
(69) Szytuła, A.; Penc, B.; Kaczorowski, D.; Arulraj, A.; Baran, S.; Stüsser, N.; Tomala, K. Magnetic and Electronic Properties of RCo_xGe_2 (R = Pr, Nd) Compounds. *J. Alloys Compd.* **2008**, *460*, 120−124.
(70) Khan, M. A.; McCandless, G. T.; Benavides, K. A.; Martin, T. J.; Palacios, A. M.; Samuel, A. W. B.; Young, D. P.; Chan, J. Y. Crystal Growth and Magnetic Properties of $Pr_3Co_{2+x}Ge_7$ and the Sn-Stabilized $Ln_3Co_{2+x}Ge_{7-y}Sn_y$ (Ln = Pr, Nd, Sm). *Cryst. Growth. Des.* **2018**, *18*, 6028−6034.
(71) Lin, X.; Bud'ko, S. L.; Thimmaiah, S.; Canfield, P. C. Anisotropic Magnetization, Resistivity and Heat Capacity of Single Crystalline $R_3Ni_{2-x}Sn_7$ (R = La, Ce, Pr and Nd). *J. Magn. Magn. Mater.* **2013**, *331*, 53−61.
(72) Harmening, T.; Eul, M.; Pöttgen, R. Nickel-deficient Stannides $Eu_2Ni_{2-x}Sn_5$ - Structure, Magnetic Properties, and Mössbauer Spectroscopic Characterization. *Z. Naturforsch. B: Chem. Sci.* **2009**, *64*, 1107−1114.
(73) Weiland, A.; Eddy, L. J.; McCandless, G. T.; Hodovanets, H.; Paglione, J.; Chan, J. Y. Refine Intervention: Characterizing Disordered $Yb_{0.5}Co_3Ge_3$. *Cryst. Growth. Des.* **2020**, *20*, 6715−6721.
(74) Moshopoulou, E. G.; Ibberson, R. M.; Sarrao, J. L.; Thompson, J. D.; Fisk, Z. Structure of Ce_2RhIn_8: An Example of Complementary Use of High-Resolution Neutron Powder Diffraction and Reciprocal-Space Mapping to Study Complex Materials. *Acta Crystallogr. B* **2006**, *62*, 173−189.
(75) Hering, E. N.; Borges, H. A.; Ramos, S. M.; Fontes, M. B.; Baggio-Saitovich, E.; Continentino, M. A.; Bittar, E. M.; Mendonça Ferreira, L.; Lora-Serrano, R.; Gandra, F. C. G.; Adriano, C.; Pagliuso, P. G.; Moreno, N. O.; Sarrao, J. L.; Thompson, J. D. Residual Superconducting Phases in The Disordered $Ce_2Rh_{1-x}Ir_xIn_8$ Alloys. *Phys. Rev. B* **2010**, *82*, 184517.
(76) Uhlířová, K.; Prokleška, J.; Sechovský, V. Comment on "Emergence of a Superconducting State from an Antiferromagnetic

https://doi.org/10.1021/acsomega.2c02152
ACS Omega 2022, 7, 19048−19057

Phase in Single Crystals of the Heavy Fermion Compound Ce_2PdIn_8". *Phys. Rev. Lett.* **2010**, *104*, 059701.
(77) Kaczorowski, D.; Pikul, A. P.; Gnida, D.; Tran, V. H. Emergence of a Superconducting State from an Antiferromagnetic Phase in Single Crystals of the Heavy Fermion Compound Ce_2PdIn_8. *Phys. Rev. Lett.* **2009**, *103*, 027003.
(78) Wirth, S.; Prots, Y.; Wedel, M.; Ernst, S.; Kirchner, S.; Fisk, Z.; Thompson, J. D.; Steglich, F.; Grin, Y. Structural Investigations of $CeIrIn_5$ and $CeCoIn_5$ on Macroscopic and Atomic Length Scales. *J. Phys. Soc. Jpn.* **2014**, *83*, 061009.
(79) Uhlířová, K.; Prokleška, J.; Sechovský, V.; Daniš, S. Solution Growth of Ce-Pd-In Single Crystals: Characterization of The Heavy-Fermion Superconductor Ce_2PdIn_8. *Intermetallics* **2010**, *18*, 2025−2029.
(80) Bao, J.-K.; Zheng, H.; Wen, J.; Ramakrishnan, S.; Zheng, H.; Jiang, J. S.; Bugaris, D.; Cao, G.; Chung, D. Y.; van Smaalen, S.; Kanatzidis, M. G. Superconductivity in Y_4RuGe_8 with a Vacancy-Ordered $CeNiSi_2$-Type Superstructure. *Chem. Mater.* **2021**, *33*, 7839
(81) Wright, C. J. C.; Dooryhée, E.; Pressley, L. A.; Phelan, W. A.; Khalifah, P. G.; Billinge, S. J. L. Toward In Situ Synchrotron Mapping of Crystal Selection Processes during Crystal Growth. *Chem. Mater.* **2021**, *33*, 3359−3367.
(82) Shoemaker, D. P.; Hu, Y.-J.; Chung, D. Y.; Halder, G. J.; Chupas, P. J.; Soderholm, L.; Mitchell, J. F.; Kanatzidis, M. G. In Situ Studies of a Platform for Metastable Inorganic Crystal Growth and Materials Discovery. *Proc. Natl. Acad. Sci. U.S.A.* **2014**, *111*, 10922−10927.
(83) Weiland, A.; Frith, M. G.; Lapidus, S. H.; Chan, J. Y. In Situ Methods for Metal-Flux Synthesis in Inert Environments. *Chem. Mater.* **2021**, *33*, 7657−7664.
(84) Schultze, D. Applications of Differential Thermal Analysis to the Preparation of Single Crystals. *Thermochim. Acta* **1991**, *190*, 77−110.
(85) Janssen, Y.; Angst, M.; Dennis, K. W.; McCallum, R. W.; Canfield, P. C. Differential Thermal Analysis and Solution Growth of Intermetallic Compounds. *J. Cryst. Growth* **2005**, *285*, 670−680.
(86) Xu, L.; Wang, Z.; Chen, J.; Chen, S.; Yang, W.; Ren, Y.; Zuo, X.; Zeng, J.; Wu, Q.; Sheng, H. Folded Network and Structural Transition in Molten Tin. *Nat. Commun.* **2022**, *13*, 126.
(87) Latturner, S. E. Clusters, Assemble: Growth of Intermetallic Compounds from Metal Flux Reactions. *Acc. Chem. Res.* **2018**, *51*, 40−48.
(88) Canfield, P.; Kong, T.; Kaluarachchi, U.; Jo, N. H. Use of Frit-disc Crucibles for Routine and Exploratory Solution Growth of Single Crystalline Samples. *Philos. Mag.* **2016**, *96*, 84−92.
(89) Krause, L.; Herbst-Irmer, R.; Sheldrick, G. M.; Stalke, D. Comparison of Silver and Molybdenum Microfocus X-Ray Sources for Single-Crystal Structure Determination. *J. Appl. Crystallogr.* **2015**, *48*, 3−10.
(90) Sheldrick, G. M. SHELXT - Integrated Space-Group and Crystal-Structure Determination. *Acta Crystallogr. A: Found. Adv.* **2015**, *71*, 3−8.
(91) Sheldrick, G. M. Crystal Structure Refinement with SHELXL. *Acta Crystallogr. C* **2015**, *71*, 3−8.

https://doi.org/10.1021/acsomega.2c02152
ACS Omega 2022, 7, 19048−19057